Aerospace Science and Technology 60 (2017) 68–83

Contents lists available at ScienceDirect

Aerospace Science and Technology

www.elsevier.com/locate/aescte

On the aero acoustic and internal flows structure in a centrifugal compressor with hub side cavity operating at off design condition

Ibrahim Shahin [a,*], Mohamed Alqaradawi [b], Mohamed Gadala [c], Osama Badr [d]

[a] Mechanical Engineering Department, Shoubra Faculty of Engineering, Benha University, Egypt
[b] Mechanical and Industrial Engineering Department, Collage of Engineering, Qatar University, Doha (2713), Qatar
[c] Mechanical Engineering Department, UBC-University of British Columbia, Vancouver, BC, Canada
[d] Mechanical Engineering Department, the French University in Egypt, Al-Shorouk City, New Cairo, Egypt

ARTICLE INFO

Article history:
Received 11 May 2016
Received in revised form 9 October 2016
Accepted 28 October 2016
Available online 11 November 2016

Keywords:
Aero-acoustic
LES
Centrifugal compressor
Hub side cavity and surge

ABSTRACT

This paper covers the characterization of the acoustic noise and the unsteady flow field of a high speed centrifugal compressor NASA CC3. In order to accurately predict the noise, all analyses are carried out through the use of Large Eddy Simulation and Ffowcs Williams–Hawkings model for noise prediction. The relative effect of hub cavity on flow characteristics and sound levels is investigated, for a compressor stage with a total pressure ratio equal to 4, working from surge to near choke condition. In comparison with the experimental results from literature, the predicted compressor performance and flow field are predicted well, some trends seen in experiments are captured. The hub cavity flow effect on the compressor aero acoustic generated noise is shown in the paper. The unsteady static pressure and sound pressure levels are compared not only at different location but also for design and off design operating points. The internal flow results inside the hub cavity are presented at surge, design and near choke points. The conclusion is that the cavity effect of the centrifugal compressor cannot be ignored in the numerical prediction of aerodynamic generated noise. The impeller back plate of the rotor experiences a strong pressure fluctuation, which is maxima at the impeller outer radius for all operating point, but higher pressure values at the surge point.

1. Introduction

The aero-acoustic analysis of turbo machines has become urgent not only due to demands requirements for environment-friendly products [1] but also to prevent compressors from mechanical failure [2]. If acoustics resonances occur within centrifugal compressor, the pressure fluctuations may reach high values which results in high cyclic fatigue. Even though compressor parts are designed for high cycle fatigue; this would jeopardize the safe operation of the compressor and the facility. Due to the progress in aero-acoustic computational methods, however, the aerodynamic/acoustic optimum design of the centrifugal compressor parts has become available. Rotating stall is an unsteady flow phenomenon in which one or more “stall cells” travel around the compressor annulus in the direction of rotation of the compressor, with a rotational speed which may reach 50% of the compressor rotational speed. Rotating stall results in a noticed vibratory stresses in the compressor rotating parts, which is unfavorable for structural issues, although the compressor may continue to give suitable performance [3]. Surge consists of large-amplitude oscillations of the flow through the entire compressor which also produces large oscillations in compressor delivery pressure [4].

The unsteady flow in centrifugal compressor has been studied by many researchers, and the unsteady flow phenomena such as stall and surge are also investigated. Mckain and Holbrook introduced the detailed design for a single stage centrifugal compressor with pressure ratio equal to 4 [5]. The data published by Skoch et al. [6] included experimental results for the internal flow velocities measured by Laser-Doppler Anemometer in the impeller of a centrifugal compressor. The results indicated that the tip clearance flow is the main source of through-flow velocity deficit in the impeller region. Wernet et al. [7] presented experimental measurements with pressure transducer, to indicate the unsteady behavior of the pressure inside centrifugal compressor just the inception of rotating stall. To capture the instantaneous velocity and pressure data during surge event, The Digital Particle Image Velocimetry was used in the vanned diffuser area. The measurements helped in understanding the stall and surge initiation in centrifugal compressor. Also, it has been used for optimizing active surge control

* Corresponding author.
E-mail addresses: Ibrahim.shahin@feng.bu.edu.eg (I. Shahin), myq@qu.edu.qa (M. Alqaradawi), gadala@mail.ubc.ca (M. Gadala), Osamaabadr@outlook.com (O. Badr).

http://dx.doi.org/10.1016/j.ast.2016.10.031
1270-9638/

Nomenclature

U_2	Impeller tip speed ..... m/s	L_S	The mixing length for sub grid scales
r	Radius..... mm	$\bar{S}_{ij}$	The rate of strain tensor for the resolved scales
R_2	Impeller outer diameter	d	The distance to the closest wall
ρ	Fluid density ..... kg/m^3	C_s	The Smagorinsky constant
u	Flow velocity vector	Δ	The local grid scale
u_i	Fluid velocity component in the x_i direction	T	Diffusion coefficient
u_n	Fluid velocity component normal to the surface	ϕ	General scalar
v_i	Surface velocity component in the x_i direction	S_ϕ	The source term of ϕ
v_n	Surface velocity component normal to the surface		
$\delta(f)$	Dirac delta function	*Abbreviations*	
$H(f)$	Heaviside function		
p'	Sound pressure at the far field	CFD	Computational fluid dynamics
T_{ij}	Lighthill stress tensor	MBPF	Main blade passing frequency
P_{ij}	Compressive stress tensor	NASA	National Aeronautics and Space Administration
u_g	Mesh velocity of the moving mesh	RMS	Root Mean Square
k	The von Karman constant	SBPF	Splitter blade passing frequency
		SPL	Sound pressure level

techniques. In fact, reviewing existing studies on aero-acoustic interaction indicates that centrifugal compressors have received less care than their axial compressor counterparts and especially in the unsteady aerodynamics flow. Interference generated in axial compressors has received much attention, due to the strict patterns in the aero-engine industry because of its aeronautical use and public demand for aircraft with lower noise [8,9]. Hanson [10] showed that under certain inlet and exit conditions, an acoustic mode could get trapped between blade rows leading to amplification and higher frequency propagation. Mengle [11] analyzed the physical aspects of spinning acoustic modes produced by blade vibration. Besides, the theoretical development is conducted to understand and anticipate the frequency spectra observed in the stationary and rotating reference frames.

Recently Semlitsch and Mihăescu [12] studied numerically the flow inside a ported shroud centrifugal compressor at stable and surge conditions. Unsteady three dimensional flow simulation was conducted with Large eddy simulation. The unsteady flow phenomena has been investigated in details by using the modal decomposition techniques. The flow structure has been analyzed in details during the surge event. Sundström et al. [13] performed a numerical study to predict the internal flow and aero-acoustic noise from a centrifugal compressor operate at stable and unstable flow rates. The noise generation mechanisms are identified in terms of noise directivity maps and sound pressure level spectra.

Raitor and Neise [14] measured aero acoustic performance and investigated the sources and mechanisms of sound generation of the spectral components governing the overall noise level of centrifugal compressors. The aero-acoustic noise sources in a centrifugal compressor are well described at low operating speed. Radial compressor noise is dominated by blade tone noise components, buzz-saw noise components and tip clearance noise (TCN) components. A blade tone noise component is generated from the rotor shaft speed harmonics and it is noticed at the BPF (blade passing frequency) and its harmonics. Buzz-saw tones are also a common noise component that characterizes compressors operating with supersonic fan tip speeds, these components are known to generate a tonal sound spectrum spread over a range of harmonics of the engine shaft rotation frequency. TCN is a narrow-band noise observed at frequencies about half the blade passing frequency (BPF).

A small number of experimental and numerical studies have been conducted on aero acoustic excitation sources in centrifugal compressor stages commonly which are applicable in the gas industry. Recently, Konig et al. [15] studied experimentally a shrouded impeller under high cycle fatigue. Two dimensional impeller with a vanned diffuser and a three dimensional impeller with a vanless diffuser were investigated. The authors described how to make coupling between the impeller vibration mode, a Tyler–Sofrin excitation resulting from RSI, and side cavities acoustic modes. The CFD results show that Tyler–Sofrin type acoustic modes can generate stronger forcing on the impeller external diameter than the vaned diffuser potential field. Turbocharger centrifugal compressor with ported shroud has been studied by Guillou et al. [16]. Flow recirculation has been investigated experimentally to reduce the instability in the flow and increasing the surge margin of centrifugal compressor. Particle image velocimetry (PIV) and dynamic pressure transducers have been used to measure the flow properties at stable and unstable operating point. The results indicated that flow recirculation improve the stability of the compressor, as it removes the reversed floe from the impeller blade tip.

Petry et al. [17,18] conducted experimental study with unsteady pressure instrumentation. Acoustic resonances in the side cavities of the centrifugal compressor stage have been characterized. The results showed that a cavity acoustic mode is excited when the Tyler–Sofrin mode and the cavity Eigen-mode have the same frequency and circumferential harmonics. Richards et al. [19] conducted experimental and unsteady CFD investigation for complex aero-acoustic interaction between the impeller and the upstream and downstream return channel vanes. However, the CFD study of Richards et al. [19] conducted only on blade row interactions and not including the hub and shroud cavities acoustic. Comprehensive descriptions and investigations of the flow between rotating and stationary discs, can be found in the work of Tuliszka-Sznitko [20,21], Gauthier et al. [22], Pellé [23] and Serre [24], but most of these studies neglected the complicated flow out from the impeller region and the unsteady flow during the surge event. Medic et al. [25] performed a numerical study using Large-eddy simulation (LES) with wall-adapting local eddy-viscosity (WALE) sub grid scale model to explain the complex turbulent flow in NACA CC3 centrifugal impeller, but the inlet and diffuser parts were neglected in this study and no validation with experiments has been conducted to ensure the accuracy of numerical solution. Comparison has been conducted between the results obtained with LES, Reynolds Averaged Navier–Stokes (RANS) turbulence models and hybrid RANS/LES approaches.

In this paper, the objectives from the present work are described in section 2. The compressor configuration and tested cases are described in section 3. In Section 4, the mathematical model

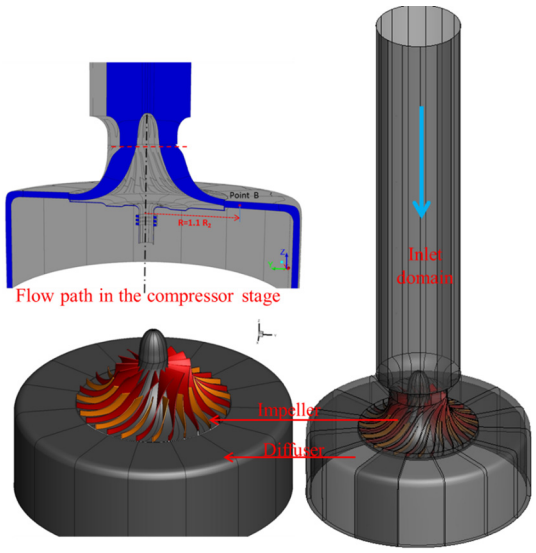

Fig. 1. The geometry of simulated parts.

is described and the verification of the present numerical model with experiments is presented also in this Section. The used aero-acoustic model is also validated and the compressor performance map is predicted and compared with experimental results. The present numerical model results are presented in Section 5, including internal flow field and sound pressure level results. Finally, conclusions and ongoing research using the 3D CFD model are commented in Section 6.

2. Scope of paper

This paper seeks to determine the physical mechanism that leads to the observed high aero-acoustic noise during the centrifugal compressor operation at off design conditions. The present paper is a continuation of a previously presented study of Shahin et al. [26] and focuses on the influence of the unsteady pressure and swirling flow in the hub side cavity on the acoustic levels. Since cavity effects are shown to be significant, in this research, a model of compressor with and without the hub cavity is proposed. Centrifugal compressor hub cavity flow simulation has been neglected by a lot of previous works, which discuss the aero acoustic simulation for centrifugal compressors [27,28].

3. Test case presentations

For the simulations performed in this work, we consider the well-studied NASA CC3 compressor that was tried over many years at the Small Engine Components Test Facility at NASA Glenn Research Center [5–7]. The mathematical model divided into stationary and moving parts which includes the inlet domain, rotating impeller and the vanless diffuser with back cavity in the impeller hub side. The shaft seal is also included to enable the model to predict the flow inside the hub cavity, shown in Fig. 1. To ensure fully developed flow condition at the compressor inlet, a straight pipe with length equals to 5 times the inlet diameter is included in the computational domain. The duct wall is included in the numerical implementation to get very accurate predictions of noise field. The impeller and diffuser dimensions are shown in Table 1. The impeller out flow is directed to a vanless diffuser with an annular radial-to-axial bend. To avoid the effect of the outlet boundary conditions on the simulated flow inside the compressor parts, compressor exit is extended in the axial direction.

Table 1
Impeller and diffuser dimensions.

Dim.	Impeller	Diffuser
No. of main blades	15	Vaneless
No. of splitter blades	15	Vaneless
Back sweep angle	50°	–
Inlet diameter	210 mm	431 mm
Outlet diameter	431 mm	810 mm
Inlet blade height	64 mm	17 mm
Exit blade height	17 mm	17 mm
Tip clearance at LE	0.154 mm	–
Tip clearance at mid chord	0.61 mm	–
Tip clearance at exit	0.203 mm	–

The studied cases are illustrated in Fig. 2, the flow path through the compressor stage is also shown. To study the effect of the hub side cavity on the internal flow and aero acoustic noise, two geometrical cases are studied. The case in which the hub cavity is included is shown in Fig. 2a, part from the impeller outlet flow go through the diffuser and the remain go through the hub cavity then through the shaft seal. The rotating wall boundary condition is used for the hub cavity wall in the impeller side, while stationary wall boundary condition is used for the hub cavity wall in the casing side. Fig. 2b shows the case without the hub cavity, the impeller exit flow is completely go through the diffuser.

4. Numerical procedures

4.1. Mathematical model

Three-dimensional, unsteady Navier–Stokes equations are solved for compressible flow. To capture the impeller rotation and the interaction between the rotating and stationary parts, the sliding mesh is assigned for the impeller fluid domain. The interface boundary conditions are used to connect the moving and station-

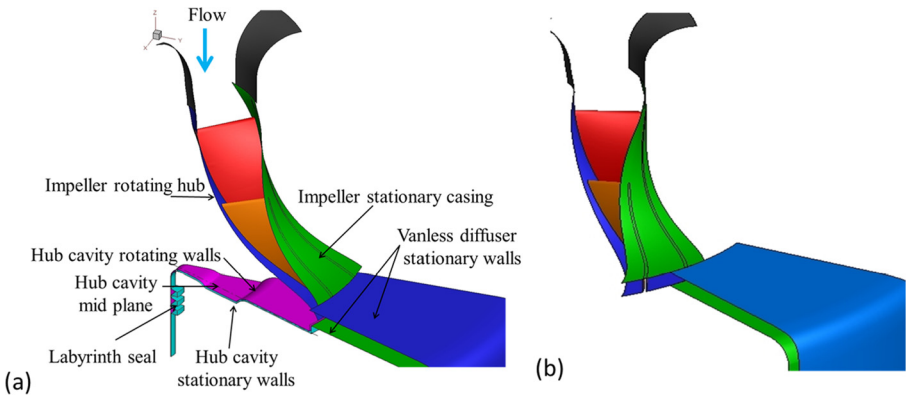

Fig. 2. Flow path in the compressor stage for: (a) with cavity, (b) without cavity.

ary cell zones. The relative position between moving and stationary domains is updated with time [29]. The general integral form of the solved conservation equation of a general scalar, ϕ, on an arbitrary control volume, V, whose boundary is moving, can be written in Eq. (1):

$$\frac{d}{d_t}\int_V \rho\phi dV + \int_{\partial V} \rho\phi(\vec{u}-\vec{u}_g).d\vec{A} = \int_{\partial V} \vartheta\nabla\phi.d\vec{A} + \int_V S_\phi dV \quad (1)$$

The unsteady large scale structures and separation zones are the main characteristics of the flow in centrifugal compressor; therefore, the large eddy simulation (LES) approach is used. In LES, large eddies are resolved directly, while small eddies are modeled with sub-grid scale model. A major role of the small scales is to dissipate the turbulent energy that is transferred from the larger scales to the smaller ones through the energy cascade. In the LES approach, the separation between the resolved and unresolved scales is achieved by low-pass spatial filtering of the governing equations. The sub grid-scale stresses resulting from the filtering operation are unknown, and require modeling by Sub-grid Scale model (SGS). The accuracy of LES simulation is essentially dependent on the SGS model in mimicking the drain associated with the energy cascade. The SGS model is used for calculating the actual eddy viscosity by extracting energy form the resolved scales. The Smagorinsky SGS model presented by Smagorinsky [30] gives a formula to determine SGS viscosity based on mixing-length type. The Smagorinsky SGS model is the original algebraic sub-grid scale model formulation. In its basic form, it is simplistic and is not computationally expensive. However, eddy-viscosity/diffusivity models, such as the Smagorinsky model are completely dissipative and it is due to this that it has inherent robustness limitations for wall-bounded flows.

The production of dynamic models has caused significant progress in the SGS modeling of turbulent flows and has removed many of the shortcomings encountered with static models Villiers [31]. Dynamic models such as purposed by Germano [32] are constructed as to permit determination of Smagorinsky "constant" as a function of both space and time. Semlitsch et al. [33] studied the effect of sub-grid stress models on the acoustic noise modeling for jet flow. Three methods were investigated, e.g. the Smagorinsky–Lilly model, a dynamic SGS model and an implicit approach. The results show that the obtained statistics are linked with the turbulent acoustic noise production. The Smagorinsky SGS model is used in this study as it has substantial published literature and validations with theory/experiments such as the work carried out by Moin and Kim [34] where analysis of fully developed turbulent channel flow was simulated numerically. Rizzetta and Visbal [35] carried out Large-eddy simulations of supersonic cavity flow fields using a high-order numerical method with a Smagorinsky derived SGS model.

In the present case, sub grid Smagorinsky–Lilly model is used, in which the eddy-viscosity is modeled by Eq. (2):

$$\mu_t = \rho L_S^2\sqrt{2\bar{S}_{ij}\bar{S}_{ij}} \quad (2)$$

where L_S is the mixing length for sub grid scales and $\bar{S}_{ij}$ is the rate of strain tensor for the resolved scales Eq. (3):

$$L_S = \min(kd, C_S\Delta) \quad (3)$$

where k is the von Karman constant, d is the distance to the closest wall, C_S is the Smagorinsky constant, and Δ is the local grid scale. In the present case, Δ is computed according to the volume of the computational cell using Eq. (4):

$$\Delta = V^{1/3} \quad (4)$$

The frequency domain approach of Ffowcs Williams–Hawkings formulation applicable to the computed domain is chosen as the governing equation for the noise prediction [36], which has been used also by [27,28] for predicting the aerodynamic noise in a centrifugal compressor. The FW–H formulation in ANSYS Fluent can handle rotating surfaces as well as stationary surfaces [29]. The FW–H equation can be written as Eq. (5):

$$\frac{1}{a_0^2}\frac{\partial^2 p'}{\partial t^2} - \nabla^2 p' = \frac{\partial^2}{\partial x_i \partial x_j}\{T_{ij}H(f)\} - \frac{\partial}{\partial x_i}\{[P_{ij}n_j + \rho u_i(u_n - v_n)]\delta(f)\} + \frac{\partial}{\partial t}\{[\rho_0 v_n + \rho(u_n - v_n)]\delta(f)\} \quad (5)$$

where:

u_i = fluid velocity component in the x_i direction
u_n = fluid velocity component normal to the surface $f = 0$
v_i = surface velocity component in the x_i direction
v_n = surface velocity component normal to the surface
$\delta(f)$ = Dirac delta function
$H(f)$ = Heaviside function
p' = the sound pressure at the far field $p = p' - p_0$
a_0 = the far-field sound speed
T_{ij} is the Light hill stress tensor, $T_{ij} = \rho u_i u_j + P_{ij} - a_0^2(\rho - \rho_0)\delta_{ij}$
P_{ij} is the compressive stress tensor, $P_{ij} = p\delta_{ij} - \mu[\frac{\partial u_i}{\partial x_j} + \frac{\partial u_j}{\partial x_i} - \frac{2}{3}\frac{\partial u_k}{\partial x_k}\delta_{ij}]$

Eq. (5) is integrated analytically under the assumptions of free space flow and the absence of obstacles between the sound sources and the receivers. The complete solution consists of surface integrals and volume integrals [29]. The surface integrals represent the contributions from monopole and dipole acoustics and partially from quadrupole sources. Propagate noise from sources to receiver by solving wave equation analytically. The surface ($f = 0$) corresponds to the source (emission) surface. In the present work, all of the solid surfaces in the domain were assigned to it as the impermeable surfaces (sources of noise) [29,54]. In the present study, the volume integrals are dropped. Thus, we have

$$p'(\vec{x},t) = p'_T(\vec{x},t) + p'_L(\vec{x},t) \quad (6)$$

where $p'_T(\vec{x},t)$ is the monopole ('thickness') noise due to unsteady volume displacement of fluid, mass injection and calculated from Eq. (7).

$$4\pi\, p'_T(\vec{x},t) = \int_{f=0}\left[\frac{\rho_0(\dot{U}_n + U_{\dot{n}})}{r(1-M_r)^2}\right]dS + \int_{f=0}\left[\frac{\rho_0 U_n\{r\dot{M}_a + a_0(M_r - M^2)\}}{r^2(1-M_r)^3}\right]d \quad (7)$$

and $p'_L(\vec{x},t)$ is the dipole ('loading') noise due to interaction of flow with moving bodies, external forces and calculated from Eq. (8)

$$4\pi\, p'_L(\vec{x},t) = \frac{1}{a_0}\int_{f=0}\left[\frac{L_r}{r(1-M_r)^2}\right]dS + \int_{f=0}\left[\frac{L_r - L_M}{r^2(1-M_r)^2}\right]dS + \frac{1}{a_0}\int_{f=0}\left[\frac{L_r\{r\dot{M}_r + a_0(M_r - M^2)\}}{r^2(1-M_r)^3}\right]ds \quad (8)$$

where

$$U_i = v_i + \frac{\rho}{\rho_0}(u_i - v_i) \quad \text{and} \quad L_i = P_{ij}\hat{n}_j + \rho u_i(u_n - v_n) \tag{9}$$

The simulation was conducted using high performance parallel computing on a server with 4 AMD Opteron processor, 48 cores and 128 GB of RAM. The ANSYS-FLUENT program with parallel processing, version 14.5 [29] was used to solve the filtered governing equations, which are discretized by the finite volume method. For the spatial discretization, a second order upwind scheme was used [37]. The second order implicit formulation was used for the temporal discretization. In order to resolve the relevant fluctuations, high grid resolution with enough small time steps were employed to have the Courant number smaller than one to be consistent with the flow properties which, for this case, give a time step of 6.119e−6 s.

The unsteady calculations are performed with a time-step size so that the impeller mesh turns less than 1° per time step, this time-step is sufficient to accurately resolve pressure spectra within human hearing range [50,51]. In LES it is desirable to make sure that no physical information can propagate further than one grid cell at one-time step. This gives a coupling between the temporal and the spatial discretization of the problem. This condition is expressed in terms the Courant Friedrichs Lewy (CFL) condition, which states that the Courant number must be less than one [38]. The sliding mesh is computationally expensive when used in rotating parts simulation, but rotor stator interaction can be predicted well. The sliding mesh technique in FLUENT has been successfully used in simulating Rotor Stator Interaction "RSI" [39–44]. Also, the blade passage effects are well captured and the position of the impeller relative to the diffuser is captured, by which the relevant fluctuations are resolved.

4.2. Boundary conditions

The mass flow inlet boundary condition is used at the inlet of the pipe with atmospheric pressure and 288 K and pressure outlet boundary condition at the domain outlet. The pressure outlet boundary condition is specified at the seal exit which equal to atmospheric pressure. Both the inlet and outlet boundaries are specified to be non-reflective to allow acoustic waves to travel out of the simulation with no effect on the solution. Acoustic reflections can be terminated either by using highly dissipative terminations or by using long ducts between the geometry to be studied and the duct ends [39]. So in the present model, along duct is used at inlet to terminate acoustic reflections. At the outlet boundary, the pressure outlet boundary condition is used with non-reflecting boundary conditions "NRBC" [29]. The cavity outlet boundary is specified as a pressure outlet boundary with non-reflecting conditions, the atmospheric pressure and temperature are specified this boundary.

In order to use the moving sliding mesh technique, the interface boundary conditions were used at the inlet and outlet of the moving and stationary parts. Rotational periodic boundary condition was used to save the calculation time. The numerical simulation of rotating stall must be performed on a full-annulus computational domain. However, the computational domain may be limited to a periodic sector if possible. This compromise allows saving much computational time, even though it forces the periodicity of the flow. The study of RSI "rotor stator interaction" and of the interactions between rotating stall cells and RSI remains possible with such a computational domain; therefore, this hypothesis can be used [45]. Wall boundary condition with no slip velocity is employed on walls. The rotating cavity face has the same rotational speed of the impeller, while the fixed cavity face has zero speed. The impeller casing wall has zero absolute speed.

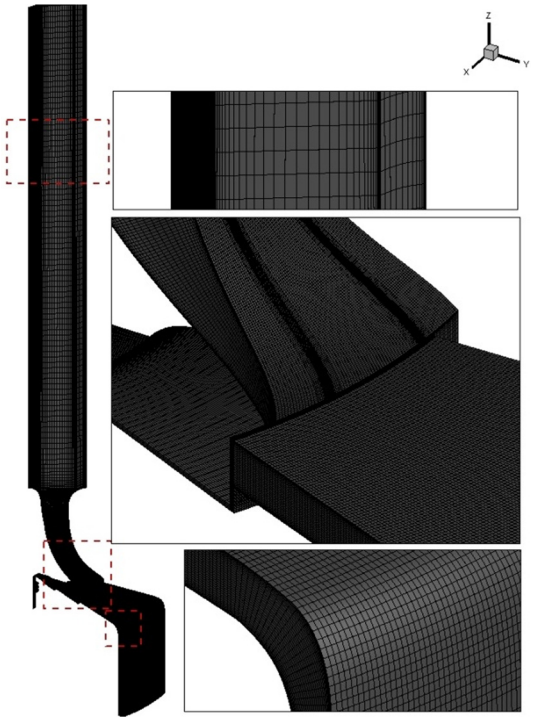

Fig. 3. Computational domain grid "3.23 Million of nodes".

Table 2
Operating conditions and unsteady simulation parameters.

Condition		Value
Design Inlet pressure	bar	1.013
Design pressure ratio		4:1
Inlet temperature	K	288
Design mass flow rate	lbm/s	10
Surge mass flow rate	lbm/s	7.2
Rotational Speed	rpm	21789
Total simulated flow time	sec	0.175
Time step	sec	6.119e−6
Number of time steps		28600
Number of iteration per time step		20
Hardware operating time per case	day	75
Number of simulated surge cycles		2

4.3. Computational grid characteristics

The ICEM CFD [21] blocking tool has been used to develop the model mesh with hexahedral element type, which consist of one blade sector. To ensure the ability of the present model to capture the boundary layers, the grid is concentrated near the walls boundaries and elements are enlarged by 5% as moved away from it. The computational grid generated for one passage is shown in Fig. 3. Sufficient number of elements has been used in the tip flow clearance to capture the effect of tip leakage flow. The grid is concentrated near the walls and the measured $y+$ is less than 1. The grid is enlarged by a ratio of 5% as it moved further away from the walls. Operating conditions and unsteady simulation parameters are listed in Table 2. In order to ensure that the used mesh has adequate density to capture turbulent flow structures in the frequency range of interest, a Mesh Frequency cut-off check was done. Ten grid points are used to resolve one acoustical wavelength [55].

4.4. Solution convergence

Two criterions have been used to judge solution convergence. The residual levels are examined and relevant integrated quantities

Table 3
Mesh arrangement descriptions.

Case	Mesh numbers	Number of elements in tip clearance	Number of elements in hub cavity height	Min grid size (mm)	Turbulence model	$y+$	Δt (s)
URANS	3.23×10^6	10	10	0.152	RNG $k-\varepsilon$	2.61	6.6e−6
LES-1	3.23×10^6	10	10	0.152	LES	2.01	6.119e−6
LES-2	4.35×10^6	10	15	0.073	LES	1.14	6.119e−6
LES-3	6.451×10^6	10	25	0.0154	LES	0.96	6.119e−6

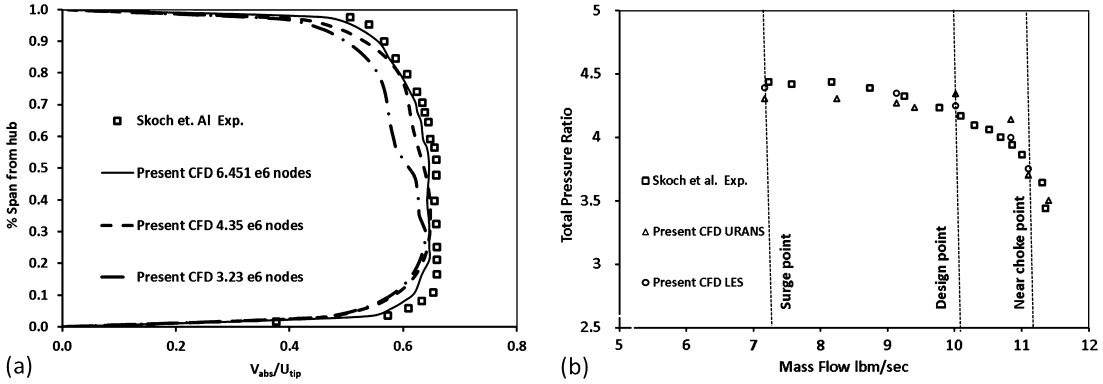

Fig. 4. Comparison of measured data [6] and present simulation: (a) velocity in the vaneless diffuser for different computational number of nodes; (b) stage performance map.

such as pressure and mass flow are also monitored during the iterations [29]. The data monitor and residual levels '1e−4' are used to judge the computation convergence for the unsteady calculations. Residuals measure imbalance (or error) in conservation Equations and usually scaled relative to the local value of the property in order to obtain a relative error. The mass flow at duct inlet, impeller inlet, impeller outlet and diffuser outlet are monitored during the calculations, also the static and dynamic pressure are monitored at different locations in the simulation domain such as impeller inlet, impeller outlet and diffuser outlet. After the solution convergence, all the flow properties are sampled for a time equal to 0.175 sec. The hardware calculation time is about 1800 hours per each case.

4.5. Mesh sensitivity study and numerical model validation

4.5.1. Flow field and performance

In order to ensure the accuracy of present numerical solution, a careful check for present numerical model was conducted. The present CFD results are compared with the experimental results from literature to verify the present numerical model. Careful check for grid independence was also conducted; three numbers of computational nodes were used 3.23, 4.36 and 6.451 million of nodes. The numbers of nodes are changed by increasing the number of elements for the impeller and diffuser in meridional, radial and spanwise directions. Mesh arrangement descriptions are shown in Table 3. The initial URANS computational mesh has about 3.23 million computational nodes. The subsequent LES grids were obtained by refining the initial grid in axial, radial and spanwise directions, first to a grid of approximately 3.23 million nodes, 4.23 million nodes, and then grid of about 6.451 million cells. Time-step size was calculated to be 6.119e−6 s. The LES simulation cases "LES-1, LES-1 and LES-3" were performed with different CFL to keep the time step constant, and consequently the number of time steps required completing one impeller revolution still constant for all cases. The LES calculations were initially tested on the low number of computational nodes, and then switched to the finer grid, and all the results presented for each case. Performance predictions with URANS simulation indicate that the losses are still under predicted compared to the LES simulation, and the LES results are more close to the experimental results.

The absolute velocities normalized by impeller tip speed at design flow rate with different number of computational nodes are shown in Fig. 4a, for Skotch et al. [6] experimental results and present CFD. The present CFD results for mesh 3.23 and 4.36 million of nodes under estimate the velocity profile after the impeller outlet, while the results with 6.451 million nodes agree well with experimental data from [6]. It is clear that the tip leakage flow is well detected, so the grid with 6.451 million nodes was used for all the studies conducted in the present simulation. The comparison between the present CFD results and experimental results from literature, indicate that the present numerical model predicts well the flow physics inside the compressor. Although the velocities predicted by CFD is slightly lower than the experimental results close to the diffuser hub and shroud walls. These differences are resulted from the smooth and the adiabatic assumption at walls. The simulation of the surge event for the centrifugal compressor is validated also in our published work [45,46] with the experiments of [47,48]. The relation between the mass flow and pressure ratio of the centrifugal compressor stage is shown in Fig. 4b for the present CFD simulation based on LES and experimental results of Skotch et al. [6]. The agreement between the computed and experimental pressure ratio is good, especially near the design point and at low-flow rates. The trend of the experimental results is well predicted by the URANS approach, but the pressure ratio is not detected well at off-design operating point especially near the stall limit. At design operating conditions, URANS slightly overestimated the pressure ratio while the results based on LES have a good agreement with the experimental results at the design operating point and at lower flow rates. The influence of tip leakage vortex and separated flow in diffuser channels is predicted well by LES more than that predicted by URANS, and this explains the disagreement between the results based on URANS and that with LES.

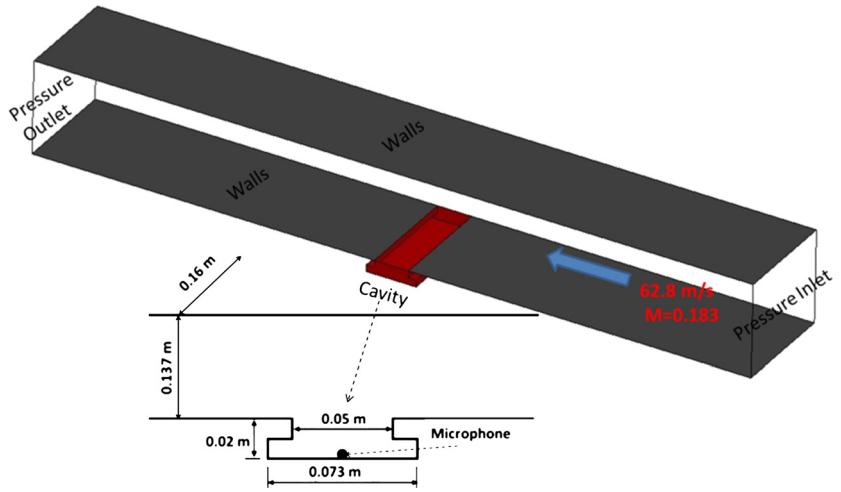

Fig. 5. Present CFD model for cavity flow.

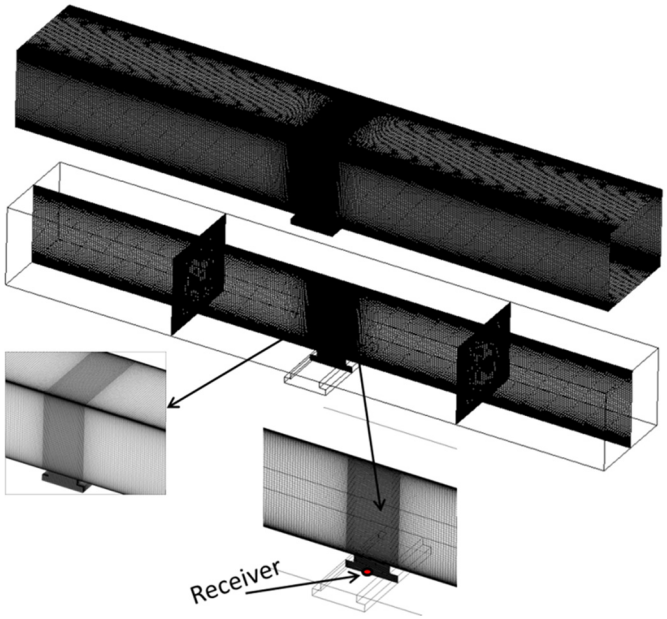

Fig. 6. Present CFD mesh used in simulating cavity flow noise.

4.5.2. Sound pressure signal validation

Cavity flow sound pressure signal validation In order to make a quantitative validation for the present acoustic model, CFD simulation for the unsteady flow past a cavity was performed to validate the sound pressure signal. Lafont et al. [49] studied experimentally the cavity flow noise of a 2D cavity for flow velocity 62.8 m/s and $M = 0.183$. The same dimensions and operating flow conditions of [49] are simulated. The simulation domain, mesh and boundary conditions are shown in Fig. 5 and Fig. 6 respectively. The studied case by Lamont et al. is a coupling between a cavity and a flow, which is similar to the cavity of the compressor. Also the velocity inlet for the present CC3 compressor is very close to that studied by Lamont et al. Fig. 7 shows the SPL signal from experiments of [49] and the same signal from the present CFD. The overall shape of the SPL spectrum is well agreed with experiment results. The two oscillations modes are predicted accurately. The signal from present CFD shows that the oscillations frequency is compared well with measurement. The average errors of the tones frequency and tones magnitude are 2.7% and 1.96%, respectively. There for, the current acoustic numerical model results are considered to be reliable.

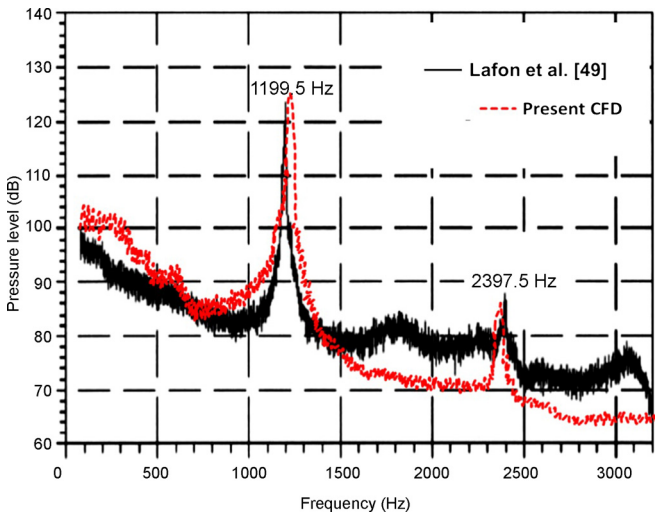

Fig. 7. Pressure level at the bottom center of the cavity for: (a) measured results (Lafon et al. [49]), (b) present CFD results.

5. Results and discussion

In the following sections, the flow physics in the mid span and near tip plans at surge, design and near choke points are presented. Also the flow field in the hub cavity region will be analyzed at these flow rates, so as to explain the reason for high SPL for lower flow rates and also for the compressor with cavity case.

5.1. Compressor impeller flow

The present study has been done at three operating conditions; surge, design and near choke conditions. The mass flow rate at impeller inlet is monitored and saved with the flow time. Fig. 8 shows the time resolved mass flow rate at the impeller inlet for the three operating points. It is clear that the fluctuation in the mass flow values are increased as the mass flow decreased. Just before the surge condition, fluctuations with higher amplitudes were detected in the mass flow. Also, the flow direction is reversed at the impeller inlet during the surge condition. This can be observed in Fig. 8a in which the mass flow at impeller inlet is monitored with the flow time. Furthermore, there is no back flow at the impeller inlet at design or near choke conditions Fig. 8b and Fig. 8c. Fluctuation with low amplitudes in the mass flow is observed with no change in the flow direction. Fig. 9 shows the

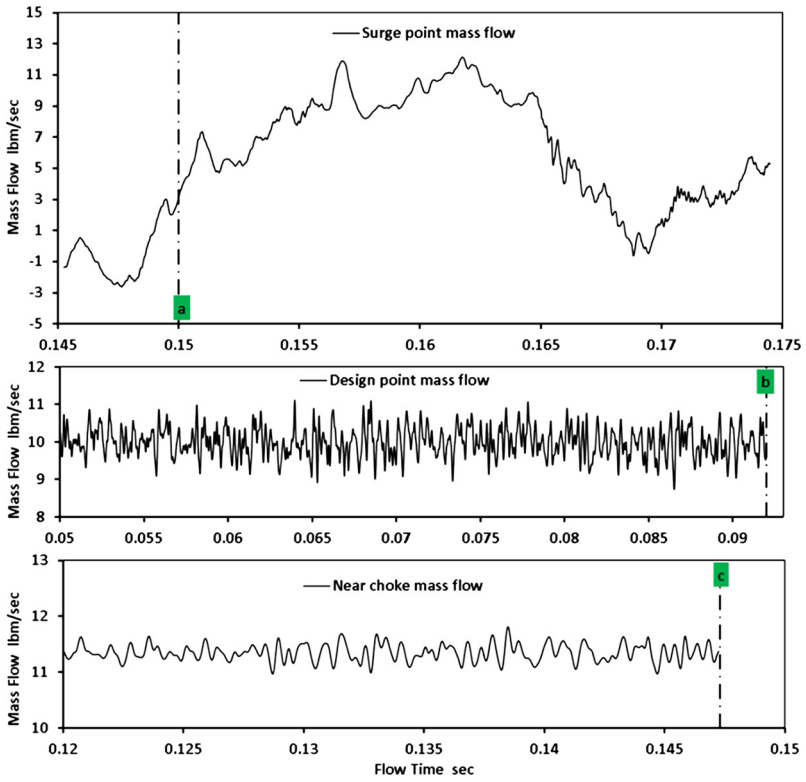

Fig. 8. Mass flow with time monitored at impeller inlet.

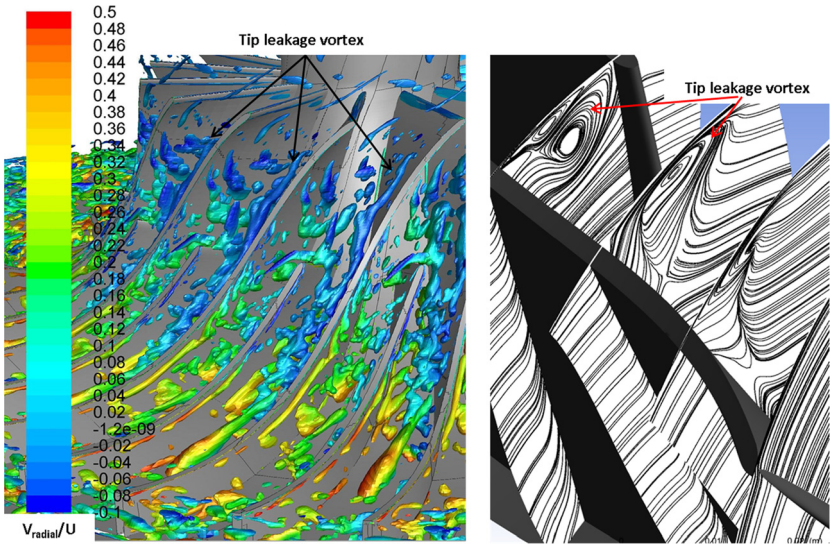

Fig. 9. Tip leakage vortex structure by: (left) normalized Q-criterion equal 0.1 colored by radial velocity; (right) stream lines at different meridional sections at the impeller inducer.

propagation of the tip leakage vortex and its structure, the tip leakage vortices are obviously detected initiated and rolling up from the leading edge and the corresponding stream lines also indicated that. The tip leakage vortex of the main blade full-blade seems to be moving from the main blade suction side towards but not reaching the next main blade pressure side.

5.2. Vaneless diffuser flow

Fig. 10a shows the vaneless diffuser core flow during surge condition and it is clear the vaneless diffusers have rotating instability that is similar to rotating stall. The rotating instabilities are characterized by a core of outward radial velocity followed by a zone of inward radial velocity, are quite well identifiable. Fig. 10b shows the absolute iso-velocity values corresponding to the design operating flow conditions. The flow pattern in the diffuser inlet is characterized by the tip leakage vortex and the jet/wake structure, which resulting from the interaction of the impeller secondary flows including the tip leakage flow. Fig. 11 shows the instantaneous static pressure at 0.5 span and 0.95 span planes, for design, surge and choke flow conditions. The pressure values are higher at 0.95 span planes more than that at 0.5 spans due to the tip leakage flow from the impeller outlet. The pressure is increased gradually from the impeller inlet to the diffuser outlet, but the pressure fluctuation is higher for design point more near chock operating point, the highest fluctuation is detected at the surge point. The rotating

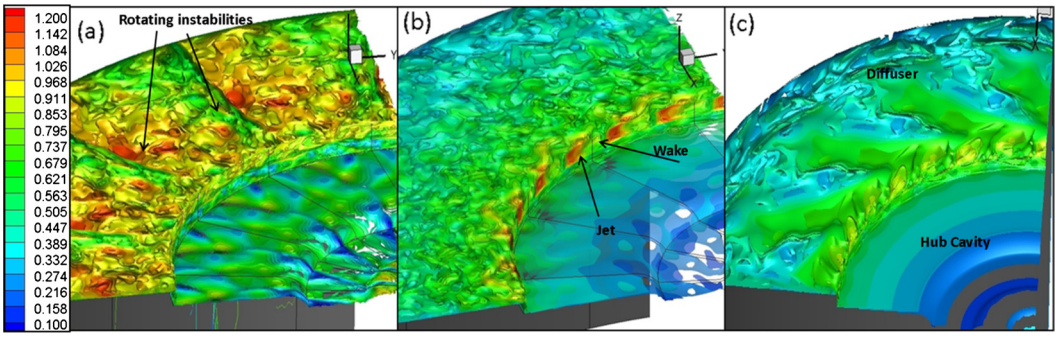

Fig. 10. Dimensionless instantaneous velocity 'V/U_2' iso-values in diffuser and hub cavity at: (a) surge, (b) design, (c) near choke.

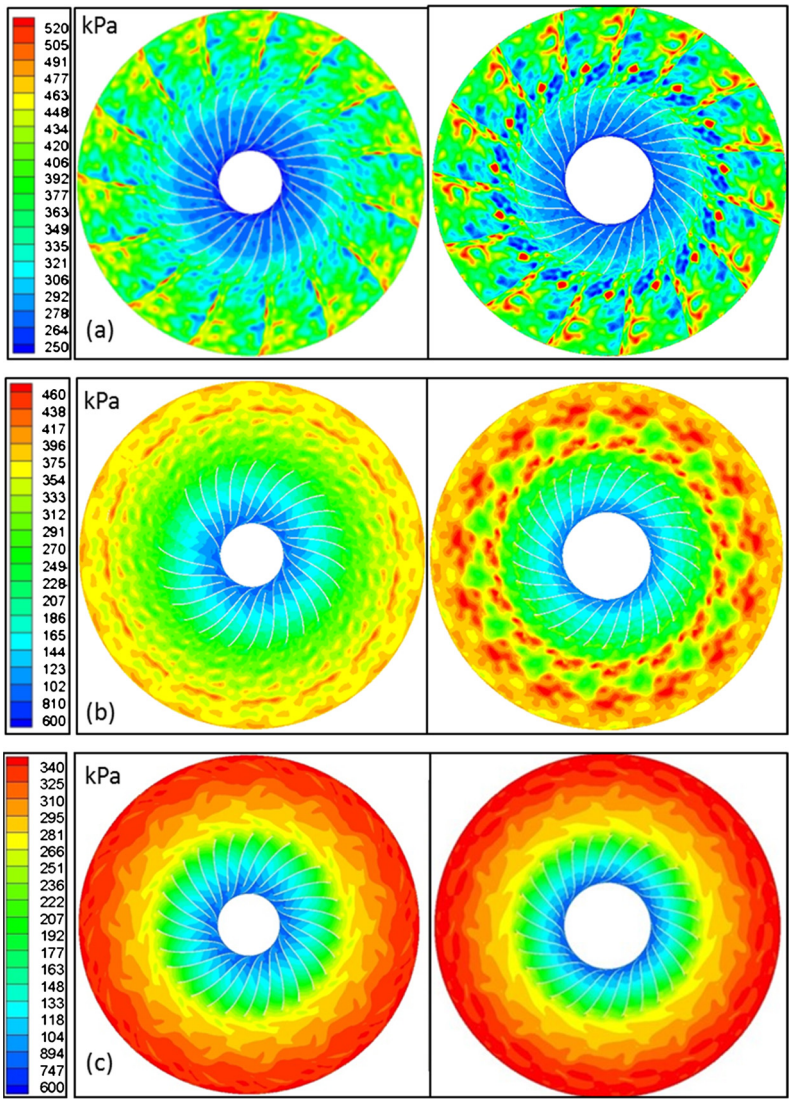

Fig. 11. Instantaneous Static pressure in kPa at: (a) surge, (b) design, (c) near choke (left: 0.5 span, right: 0.95 span).

flow instability in the diffuser and flow reversal in the impeller are the main reasons for higher pressure fluctuation.

The instantaneous radial velocity is shown in Fig. 12 for different operating flow rats. The aerodynamic behavior in the diffuser is strongly changed by moving from design operating point towards left and right in the compressor performance map. For the surge operating condition, the low momentum zone appears along the diffuser hub side and continues downstream up to the diffuser end. This is due to the impeller outlet fluid removal through the back face cavity, and the flow is aspirated through the cavity. Separation zones near the casing just after the impeller outlet are detected as a result from the impeller tip leakage flow and the flow tends to separate close to the diffuser end due to the diffusion inside the diffuser. Close to choke operating point, the influence of hub cavity leakage flows is much smaller and lower separated regions are detected. The main flow is pushed towards the casing side, as a result from the swirling flow coming to the diffuser domain from the hub cavity. Consequently, a low momentum flow

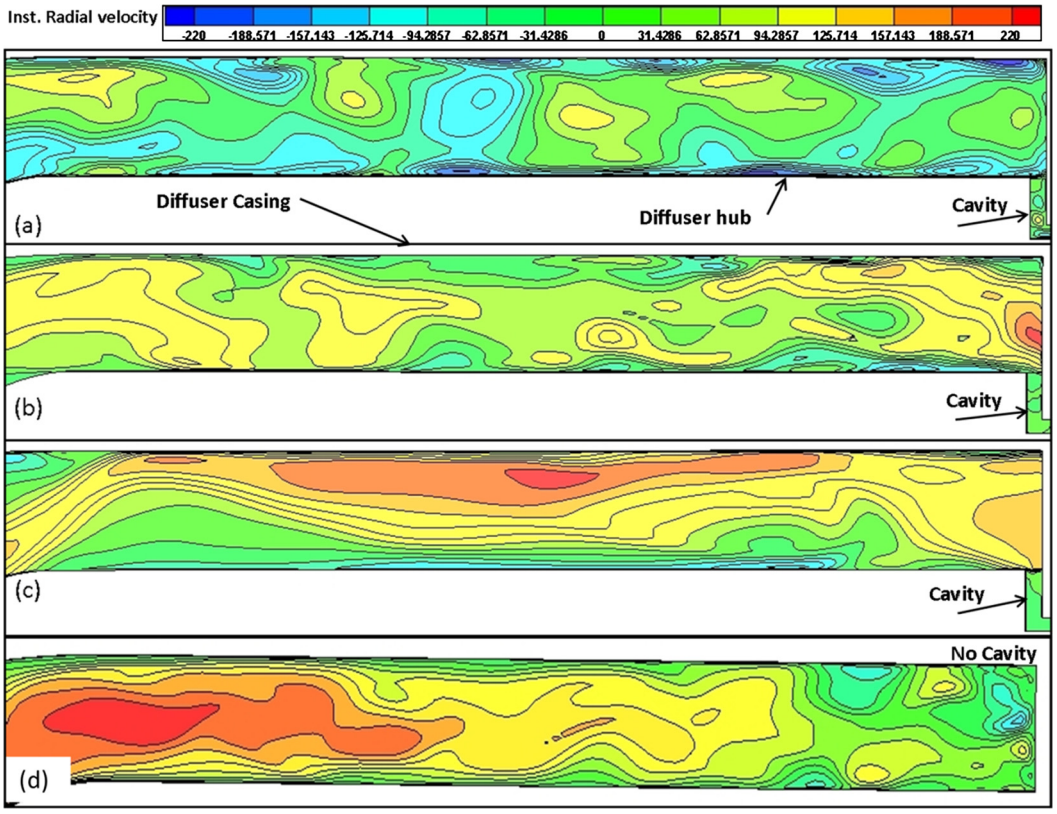

Fig. 12. Instantaneous radial velocity at diffuser for: (a) surge, (b) design, (c) near choke, and (d) no cavity case at design point.

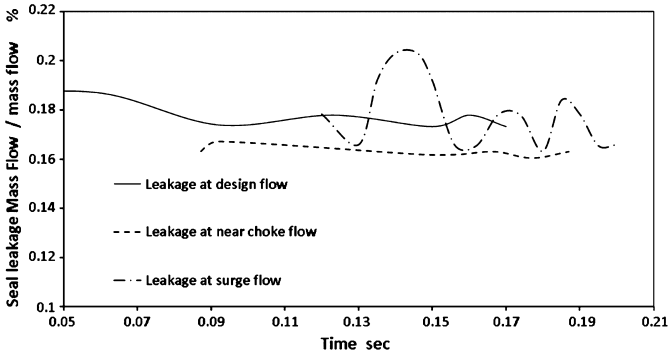

Fig. 13. Leakage flow through the hub cavity with time.

close to the hub appeared due to the removal of the mainstream flow into the hub cavity flow. The radial velocity for the no cavity case is shown in Fig. 12d, it is clear that radial velocity is increase than that in Fig. 12b as no flow extracted through the cavity, also no flow separation is detected at the diffuser hub due to the absence of the cavity. The absence of flow separation near the cavity will results in low acoustic noise when compared with case with cavity.

5.3. Hub cavity flow

Fig. 13 shows the leakage flow through the hub cavity as a percentage of the operating mass flow during the simulation time. The amount of mass flow passing through the hub cavity depends on pressure recovery and total pressure losses of downstream stationary parts. Changing the flow from the design operating point towards surge and choke affects the amount of flow through the cavity. The hub cavity flow rate is increased as surge condition, as the pressure loss is increased in the diffuser and flow blockage. Leakage flow in the hub cavity tends to decrease at near choke conditions as the pressure recovery in the diffuser is decreased. The amount of flow passing through the cavities depends, for certain geometry, on the combined effects of pressure recovery and total pressure losses of downstream stationary components for the hub one. Moving from design operating point to lower or higher flow rates point, the amount of flow through the cavity tends to increase and decrease, respectively.

The instantaneous radial velocity at hub cavity mid plan is shown in Figs. 14. Large-scale rotating structures have been observed inside the cavity for the different operating conditions. The generation of rotating pressure patterns due to the interaction between rotating and stationary components is shown in Fig. 15 and Fig. 16. The instantaneous distribution of such pressure pattern is shown for the impeller back plate and the casing. It can be seen that the impeller back plate of the rotor experiences a strong pressure fluctuation. The pressure maxima are located at the impeller outer radius all operating point, but higher pressure values are generated for the surge point. The plots show that instantaneous static pressure is greatest near the impeller trailing edge, with a significant increase in loading values when moving from near choke towards the surge point. The tip leakage vortices at the impeller exit plane is one of reasons causes a noticed increase of noise downstream of the impeller. The fluctuated flow during the surge point also causes a fluctuation on the cavity flow, which results in rotating flow instability inside the cavity and an increase for the static pressure fluctuation. The instantaneous pressure in the cavities is much higher than that on the compressor casing.

5.4. Unsteady "RMS" static pressure on compressor walls

The static pressure fluctuation on the compressor walls is presented in Fig. 17 for the three operating points. The high pressure

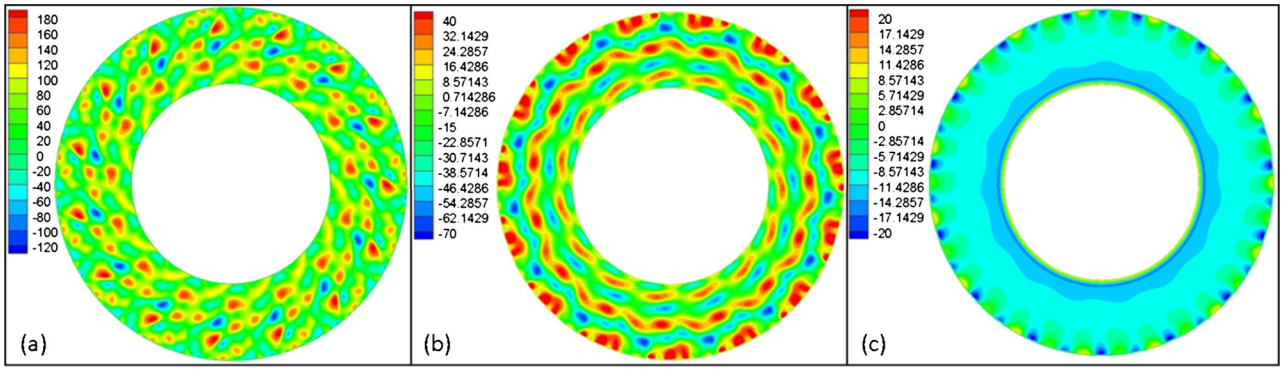

Fig. 14. Instantaneous radial velocity at hub cavity mid plan in m/sec at: (a) surge, (b) design, (c) near choke.

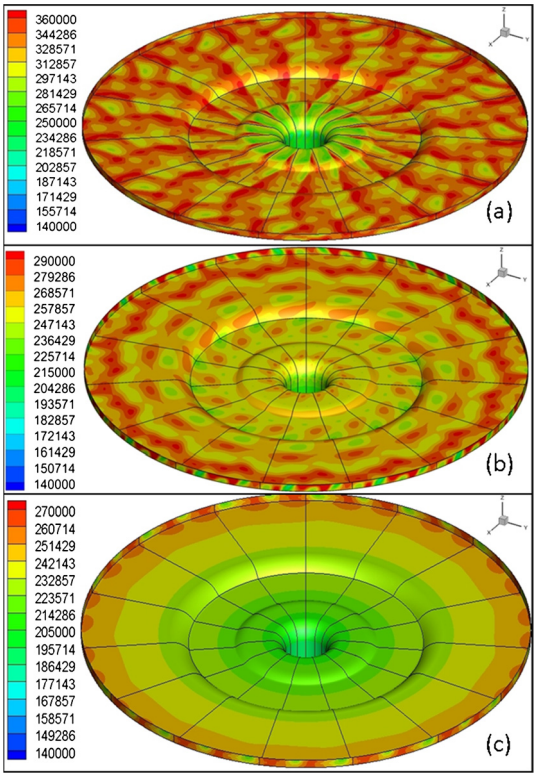

Fig. 15. Instantaneous static pressure in Pa on the impeller back plate at: (a) surge, (b) design, (c) near choke.

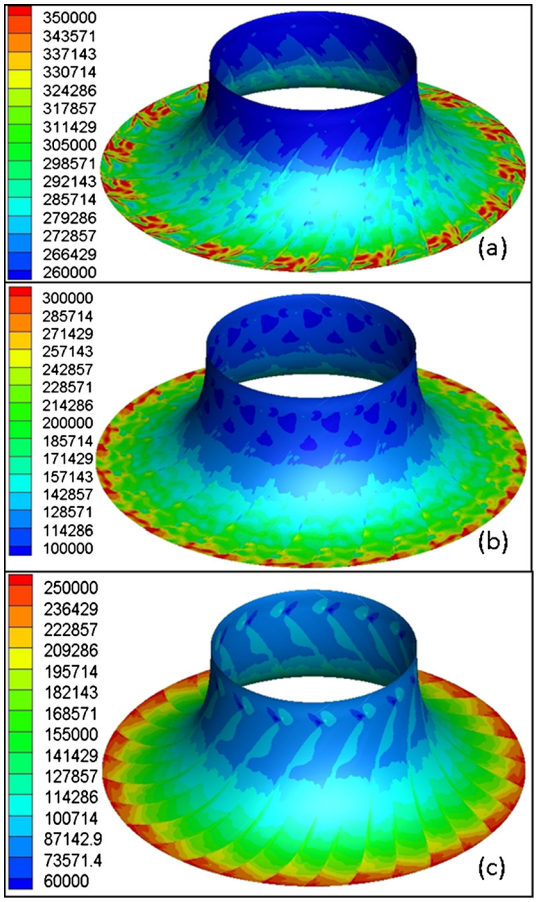

Fig. 16. Instantaneous static pressure in Pa on the impeller casing side at: (a) surge, (b) design, (c) near choke.

fluctuation at surge condition is clearly visible when compared with the design and choke points. The RMS static pressure is maximum at the vanless diffuser area, resulting from the rotor-stator integration "RSI" and rotating stall at the surge point. The impeller surfaces also have high pressure fluctuation due to the flow reversal and inner recirculation happened during the surge event, the flow reversal and inner recirculation during surge are presented and analyzed by the authors in [26,45]. The high value of pressure fluctuation during surge condition causes a noticed increase in the generated noise especially at low frequencies. The blades tip also has high values of RMS static pressure as a result from the tip leakage flow vortices; the tip clearance effect on the noise generated at near surge condition is studied by [51]. The RSI at design and choke operating point represents the highest source of pressure fluctuation. The RMS static pressure at the compressor outlet side is higher than that in the inlet side, which will cause higher aerodynamic noise to be generated in the compressor discharge side.

5.5. Spectral characteristics of compressor pressure signals

The unsteady static pressure after the impeller exit ($r = 1.1R_2$) is monitored with flow time, at that location the pressure signal obtained is not affected by the blade loading but it is still nearby impeller outlet and the jet-wake pattern still persist. The pressure signal from the time domain is converted into the frequency domain by Fast Fourier Transformation (FFT) in order to understand the intensity of interaction in the flow field. Fig. 18 shows the FFT analysis of the pressure signal at design, near stall and surge operating point. At the design flow, the peak value occurs corresponding to the blade passing frequency (BPF). Smaller spikes are observed at a lower frequency of 0.3 BPF. When the mass flow

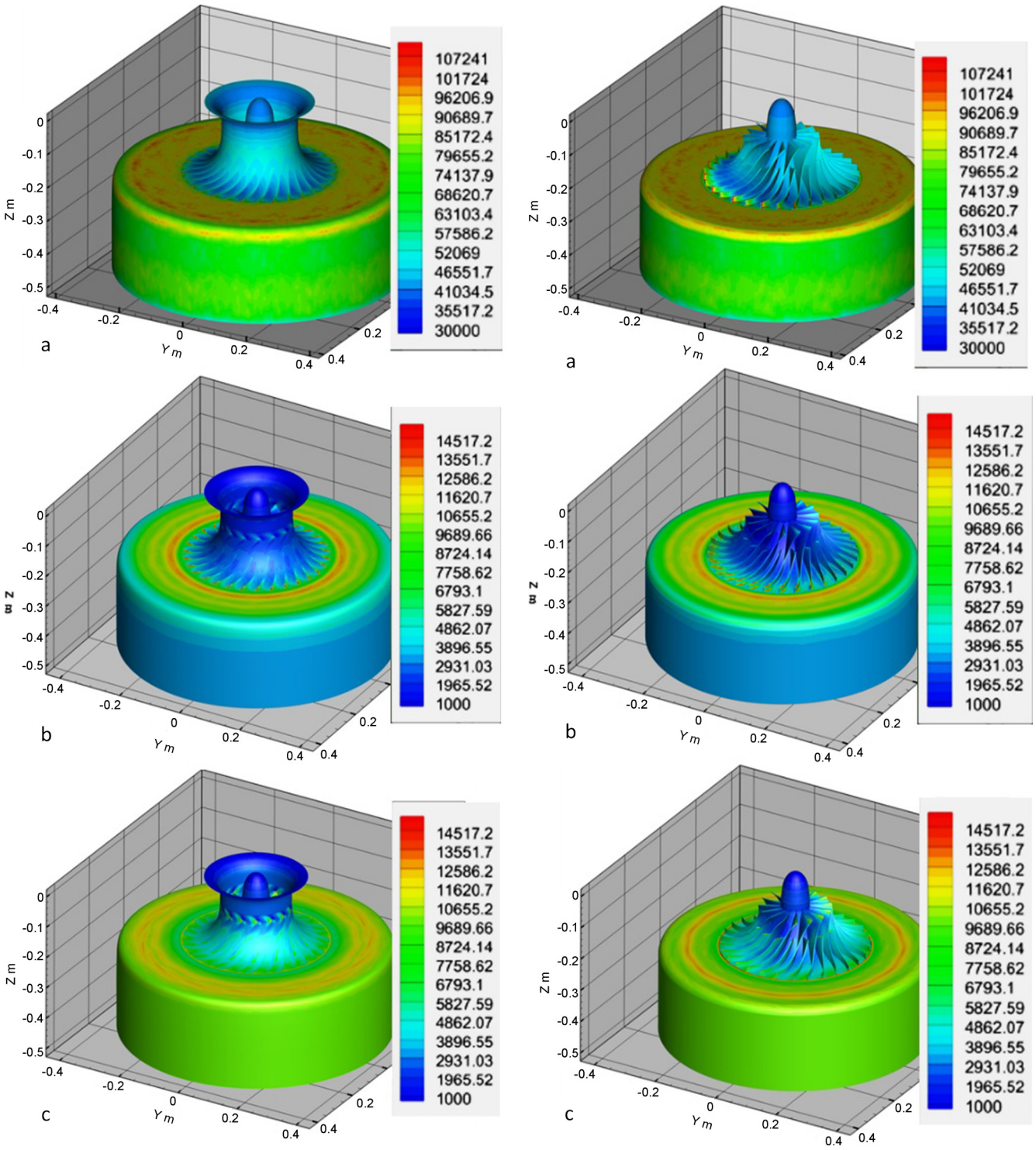

Fig. 17. Unsteady "RMS" static pressure in Pa on compressor casing "Left" and hub "Right' at: (a) surge, (b) design, (c) near choke.

is reduced to near stall flow, the FFT yields different results. The peaks are observed at a lower frequency of 0.056 BPF. This point lies near stalling region; hence the unsteadiness includes largely aperiodic components. When the mass flow is reduced further to surge point, the surge frequency becomes dominant; the increasing of the magnitude is caused by the high oscillation of the main flow pressure along the compression system, which is at a very low frequency.

5.6. Spectral characteristics of compressor noise

5.6.1. Signal de-nosing approach

The sound pressure signal at all receivers are filtered using wavelet technique, discrete wavelet transform (DWT) has been recognized as the most powerful and promising tool for partial discharge signal de-noising because it captures both time and frequency domains information [52].

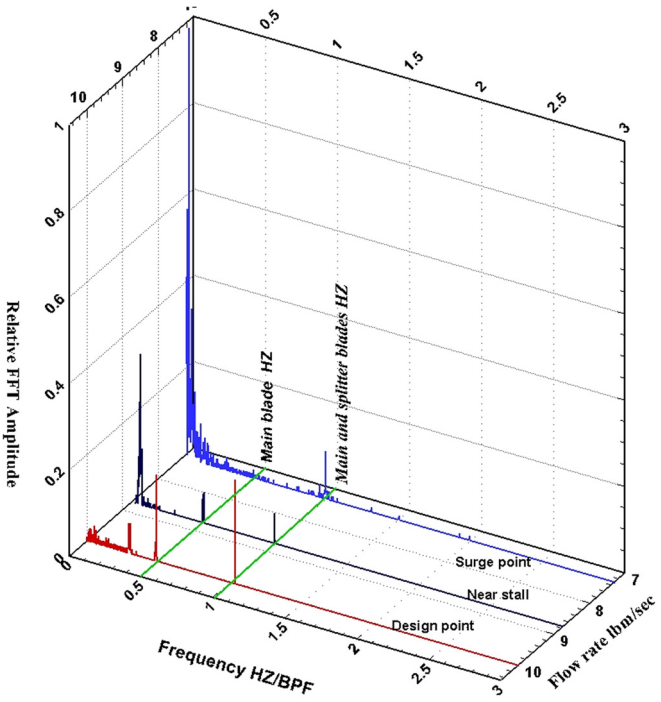

Fig. 18. Spectral analysis of pressure signals based on LES at point $1.1R_2$ for design flow, near stall and operating point.

The procedure of de-noising the signals using DWT can be summarized as follows:

a. Decomposition

Using a wavelet family, filter length, and decomposition levels as used by [53], the approximation coefficients, $a_{j,k}$ and detail coefficients, $d_{j,k}$ have been computed at levels from 1 to J as follows,

$$a_{j,k} = \langle x(i), \varphi_{j,k}(i) \rangle$$

where the scaling function $\varphi(i)$ is used to provide an approximation of $x(i)$ at a scale j; where j is an arbitrary scale. The wavelet function, $\Psi(i)$, is used in the computation of the details of $x(i)$ as follows,

$$d_{j,k} = \langle x(i), \Psi_{j,k}(x) \rangle$$

The DWT implements equations (1) and (2) using a tree composed of low pass and high pass finite impulse response (FIR) filters [56].

b. Thresholding

For each decomposition level, the threshold has been assigned for a typical value and the wavelet de-noising has been carried out using either hard or soft thresholding.

B.1 Hard thresholding

It has been developed by [57]. It processes data in such a way that the elements whose absolute values are greater than the threshold are kept and those less than or equal are set to zero.

$$\delta\lambda^{\text{Hard}}(x) = \begin{cases} x & \text{if } |x| > \lambda \\ 0 & \text{if } |x| \leq \lambda \end{cases}$$

B.2 Soft thresholding

It sets the elements whose absolute values lower than the threshold to zero and shrink the other elements towards zero.

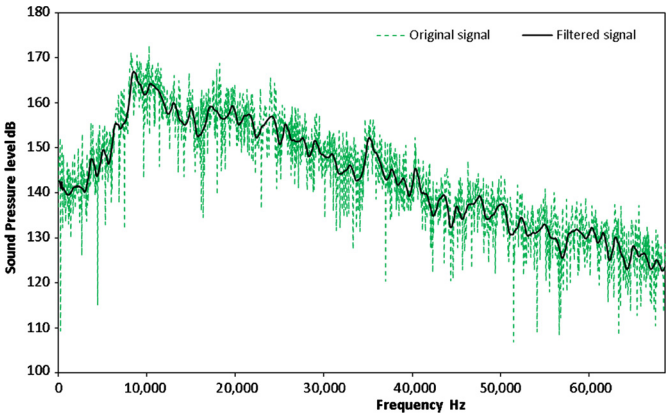

Fig. 19. Comparison between the original SPL signal and the filtered signal.

$$\delta\lambda^{\text{Soft}}(x) = \begin{cases} x - \lambda & \text{if } |x| > \lambda \\ 0 & \text{if } |x| \leq \lambda \\ x + \lambda & \text{if } |x| < -\lambda \end{cases}$$

B.3 Reconstruction

The original approximation coefficients and the shrieked detail coefficients have been utilized to apply inverse discrete wavelet transform (IDWT) and obtain the de-noised signal,

$$y(i) = \sum_k a_{j,k}\varphi_{j,k}(x) + \sum_j \sum_k d_j(k)\Psi_{j,k}(x)$$

where $y(i)$ is the denoised signal.

Fig. 19 shows a comparison between the original SPL signal and the filtered signal using DWT.

5.6.2. Sound pressure level signal analysis

The acoustic pressure signals were captured at the inlet side and discharge side of the compressor. The SPL is monitored and captured during one complete surge cycles for the surge operating conditions. These signals were computed in time domain and then converted to the frequency domain using the FFT algorithm. Sound pressure receiver locations relative to compressor parts are shown in Fig. 20. All the receivers are located on the compressor rotation axis and z represents the distance on compressor axis measured from the compressor nose which represents the zero value for z, positive values of z correspond to the inlet side while negative z corresponds to the discharge side. The receivers on the discharge side are located outside the CFD domain, and this is agreed by ANSYS FLUENT [29]. In Fig. 21 the sound pressure spectra monitored during simulation at compressor suction and discharge receivers are plotted. The x axis represents the frequency normalized by the BPF (blade passing frequency, 10895 Hz).

The BPF sound level component is seen obviously in the spectrum with high magnitudes. With increasing BPF harmonic order, the levels of the blade tone harmonics become smaller, and they decay at high frequency levels. The receiver position has a big effect on the SPL levels. As the receiver becomes close to the impeller outlet, the more noticeable are the BPF and its harmonics. Other noise component is observed at about half the BPF; this component magnitude is lower than the BPF level. It is produced by the tip leakage flow through the gap between the compressor casing and the impeller blade tips “tip clearance noise” (TCN), as observed by [10]. The sound pressure level spectra monitored on the compressor discharge side is higher than that measured in the

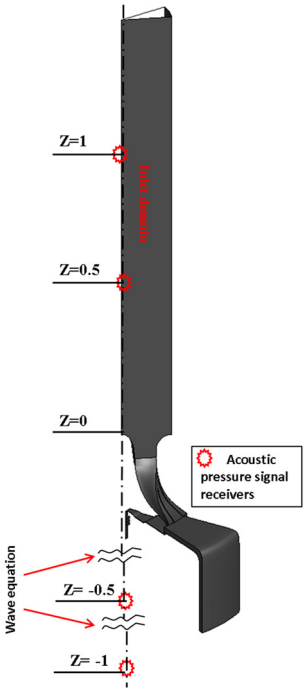

Fig. 20. Sound pressure receiver locations relative to compressor parts.

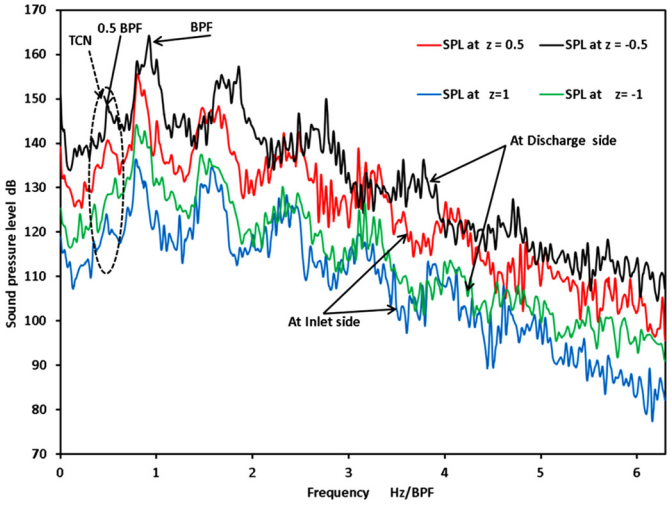

Fig. 21. Sound pressure spectra for no cavity case at different locations.

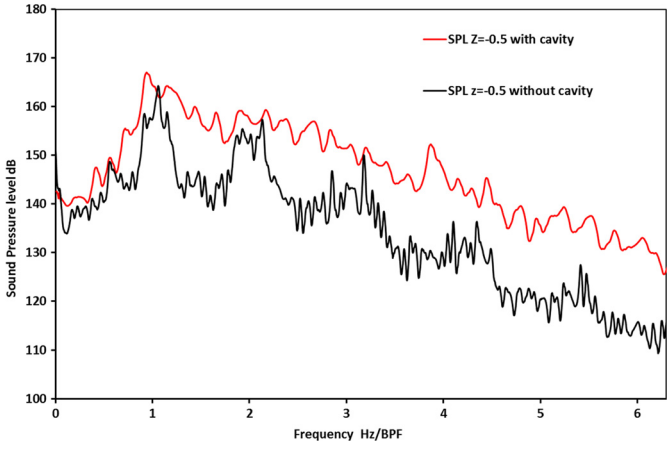

Fig. 22. Sound pressure spectra for case with and without cavity $z = -0.5$, for design point.

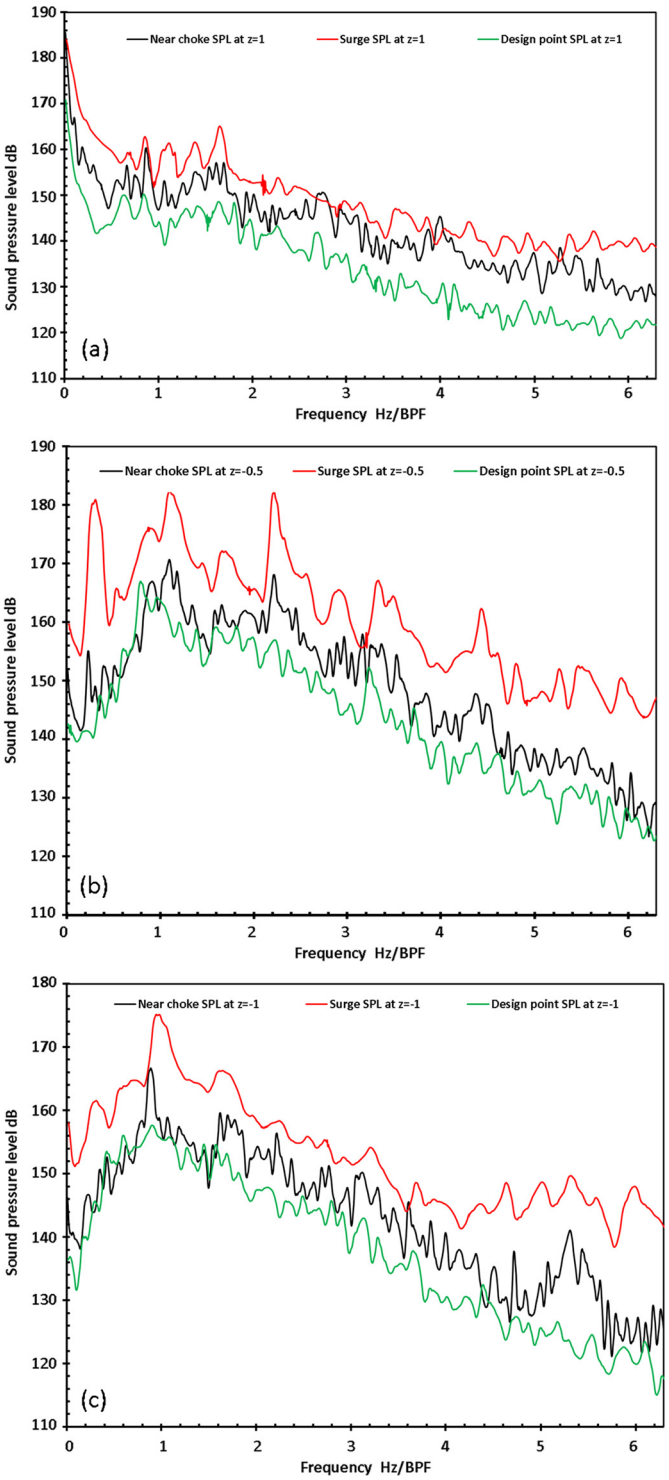

Fig. 23. Sound pressure spectra for operating point for compressor with cavity at (a) $z = 1$, (b) $z = -5$ and (c) $z = -1$.

inlet side, because noise components generated at the interface between impeller exit and stationary parts “diffuser inlet” could not transferred through the complicated flow fields in the rotor blade channels to the compressor inlet side. The pressure spectra at inlet and outlet ducts of a turbocharger compressor are measured by [47,48], the results shown that all pressure spectral at outlet duct is higher than that measured at the inlet.

Sound pressure spectra for the compressor with and without hub cavity are compared in Fig. 22. The SPL for the cavity case

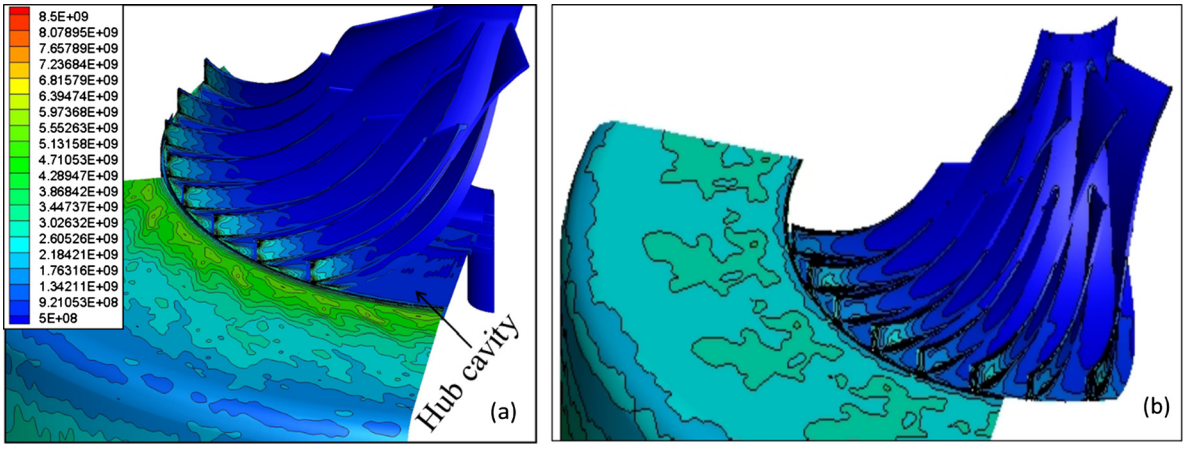

Fig. 24. Surface dpdt RMS on compressor stage walls for: (a) with cavity, (b) without cavity.

is higher than that without cavity. This difference is increased at higher frequencies. The flow swirling and high rotating pressure generated in the hub cavity is the cause of this difference, which has been shown in this paper before (Section 5.3) that the flow in the hub cavity is characterized by high swirling flow. Fig. 23 compares the SPL spectra of the compressor working from surging to near choking conditions under full speed. The spectra for different operating flow rates are presented in Figs. 23, the compressor produces sound with significant changes as the mass flow varies. The SPL at surge condition is the maximum for all receiver positions.

The surface dpdt RMS on compressor stage walls is shown in Fig. 24, for case with the hub cavity and without cavity. Fig. 24(a) gives the dpdt RMS on the impeller and diffuser huh for the case with the hub cavity, it is found that the region with highest dpdt RMS is located at the gap between impeller and diffuser. The flow separated in the diffuser inlet due to the existence of the cavity intake causes a high acoustic source. While in Fig. 24(b) the hub cavity flow is neglected and it is clear that the dpdt RMS values is decreased when compared with the case with the hub cavity. Wall with high source intensity is still near the impeller outlet and leakage clearance region. The highest surface dpdt RMS is located in the rotor-stator interaction region and after the hub cavity intake. The leakage clearance and hub cavity geometries should be improved to reduce the strength of the vortex, which will result in a decrease in the acoustic noise source.

6. Conclusions

In this paper, we examined the aerodynamic and aero acoustics performance of a transonic centrifugal compressor working from surge to near choke conditions. The effect of hub cavity on the flow characteristics and sound levels is investigated numerically. Three dimensional simulations for the compressor with and without hub cavity are performed. The entire compressible flow inside the centrifugal compressor stage is simulated through the use of LES, and Ffowcs Williams–Hawkings model for noise prediction. FFT analysis for the static pressure and acoustic signals at design flow rate indicated that, the peak value occurs corresponding to the blade passing frequency. When the mass flow is reduced further to surge point, the surge frequency becomes dominant and high SPL is detected also at low frequencies.

The SPL for the cavity case is more eminent than that without cavity, this difference increases at higher frequencies. The flow swirling and high rotating pressure generated in the hub cavity may be the reason of this conflict. The results also demonstrate that, the vaneless diffuser during surge have a rotating instability that is similar to rotating stall. The hub cavity flow rate is increased at surge condition, as the pressure losses is increased in the diffuser and flow blockage. The impeller back plate of the rotor experiences a strong pressure fluctuation higher than that detected on the shroud, which results in a generation of axial force on the impeller. The pressure maxima are located at the junction of the impeller and diffuser for all operating point, but higher pressure values are brought forth from the surge point. The propagation of rotating pressure patterns in the hub cavity is due to the interaction between rotating and stationary parts. Finally, the research done here gives a details on the hub side cavity effect on the acoustic sources for the centrifugal compressor and shows the importance of simulating the impeller cavities when deal with the compressor acoustics. The cavities of the centrifugal compressor should be included in the mathematical prediction of the noise.

Conflict of interest statement

There is no conflict of interest.

Acknowledgements

This publication was made possible by NPRP grant No. 4-651-2-242 from the Qatar National Research Fund (a member of Qatar Foundation). The statements made herein are solely the responsibility of the authors.

References

[1] D. Gottlob, Regulations for community noise, Noise News Int. 3 (4) (1995) 223–236.
[2] S. König, N. Petry, N.G. Wagner, Aeroacoustic phenomena in high-pressure centrifugal compressors—a possible root cause for impeller failures, in: Proceedings of the 38th Turbomachinery Symposium, 2009, pp. 103–121.
[3] A.H. Stenning, Rotating stall and surge, J. Fluids Eng. 102 (1) (1980) 14–20.
[4] H.W. Emmons, C.E. Pearson, H.P. Grant, Compressor surge and stall propagation, Trans. Am. Soc. Mech. Eng. 77 (4) (1955) 455–469.
[5] T.F. McKain, G.J. Holbrook, Coordinates for a High Performance 4:1 Pressure Ratio Centrifugal Compressor, Lewis Research Center, 1997, NASA-23268.
[6] G.J. Skoch, P.S. Prahst, M.P. Wernet, J.R. Wood, A.J. Strazisar, Laser anemometer measurements of the flow field in a 4:1 pressure ratio centrifugal impeller, in: ASME 1997 International Gas Turbine and Aero Engine Congress and Exhibition, American Society of Mechanical Engineers, June 1997, V001T03A049.
[7] M.P. Wernet, M.M. Bright, G.J. Skoch, An investigation of surge in a high-speed centrifugal compressor using digital PIV, J. Turbomach. 123 (2) (2001) 418–428.
[8] F. Holste, W. Neise, Noise source identification in a propfan model by means of acoustical near field measurements, J. Sound Vib. 203 (4) (1997) 641–665.
[9] J.M. Tyler, T.G. Sofrin, Axial Flow Compressor Noise Studies, 1962, SAE Technical Paper No. 620532.
[10] D.B. Hanson, Mode Trapping in Coupled 2D Cascades—Acoustic and Aerodynamic Results, AIAA Paper, (93-4417), 1993.
[11] V.G. Mengle, Acoustic spectra and detection of vibrating rotor blades, including row-to-row interference, in: AIAA, Space Programs and Technologies Conference, vol. 1, October 1990.

[12] B. Semlitsch, M. Mihăescu, Flow phenomena leading to surge in a centrifugal compressor, Energy 103 (2016) 572–587.
[13] E. Sundström, B. Semlitsch, M. Mihaescu, Centrifugal Compressor: The Sound of Surge, 2015, AIAA2015-2674.
[14] T. Raitor, W. Neise, Sound generation in centrifugal compressors, J. Sound Vib. 314 (3) (2008) 738–756.
[15] S. Konig, Acoustic eigenmodes in the side cavities of centrifugal compressors, in: ASME Turbo Expo 2009: Power for Land, Sea, and Air, American Society of Mechanical Engineers, January 2009, pp. 547–557.
[16] E. Guillou, M. Gancedo, E. Gutmark, Experimental investigation of flow instability in a turbocharger ported shroud compressor, J. Turbomach. 138 (6) (2016) 061002.
[17] N. Petry, F.K. Benra, S. Koenig, Experimental study of acoustic resonances in the side cavities of a high-pressure centrifugal compressor excited by rotor/stator interaction, in: ASME Turbo Expo 2010: Power for Land, Sea, and Air, American Society of Mechanical Engineers, October 2010, pp. 2339–2351.
[18] N. Petry, S. König, F.K. Benra, Influence of the swirling flow in the side cavities of a high-pressure centrifugal compressor on the characteristics of excited acoustic modes, J. Turbomach. 135 (3) (2013) 031024.
[19] S.K. Richards, K. Ramakrishnan, C.M. Shieh, F. Moyroud, A. Picavet, V. Ballarini, V. Michelassi, Unsteady acoustic forcing on an impeller due to coupled blade row interactions, J. Turbomach. 134 (6) (2012) 061014.
[20] E. Tuliszka-Sznitko, A. Zieliński, DNS/LES of transitional flow in rotating cavity, Int. J. Transp. Phenom. 10 (3) (2008).
[21] E. Tuliszka-Sznitko, A. Zielinski, W. Majchrowski, Large eddy simulation of non-isothermal flow in rotor/stator cavity, 2009, ICHMT digital library online.
[22] G. Gauthier, P. Gondret, F. Moisy, M. Rabaud, Instabilities in the flow between co- and counter-rotating disks, J. Fluid Mech. 473 (2002) 1–21.
[23] J. Pellé, S. Harmand, Heat transfer measurements in an opened rotor–stator system air-gap, Exp. Therm. Fluid Sci. 31 (3) (2007) 165–180.
[24] E. Serre, E. Crespo Del Arco, P. Bontoux, Annular and spiral patterns in flows between rotating and stationary discs, J. Fluid Mech. 434 (2001) 65–100.
[25] G. Medic, J. Feng, L. Chen, O. Sharma, Towards large-eddy simulation of turbulent flow in a centrifugal impeller, in: ASME 2011 Turbo Expo: Turbine Technical Conference and Exposition, American Society of Mechanical Engineers, January 2011, pp. 2057–2066.
[26] I. Shahin, M. Gadala, M. Alqaradawi, O. Badr, Unsteady CFD simulation for high speed centrifugal compressor operating near surge, in: ASME Turbo Expo 2014: Turbine Technical Conference and Exposition, American Society of Mechanical Engineers, June 2014, V02DT44A045.
[27] P. Wang, M. Zangeneh, Aerodynamic and aeroacoustic optimization of a transonic centrifugal compressor, in: ASME Turbo Expo 2014: Turbine Technical Conference and Exposition, American Society of Mechanical Engineers, June 2014, V02AT41A012.
[28] H. Sun, H. Shin, S. Lee, Analysis and optimization of aerodynamic noise in a centrifugal compressor, J. Sound Vib. 289 (4) (2006) 999–1018.
[29] ANSYS, Academic Research Release 14.5, Theory Manual, ANSYS, Irvine CA, 2012.
[30] J. Smagorinsky, General circulation experiments with the primitive equations, I: the basic experiment, Mon. Weather Rev. 91 (3) (1963) 99–164.
[31] E. De Villiers, The Potential of Large Eddy Simulation for the Modeling of Wall Bounded Flows, Doctoral Dissertation, University of London, 2007.
[32] M. Germano, U. Piomelli, P. Moin, W.H. Cabot, A dynamic subgrid-scale eddy viscosity model, Phys. Fluids A, Fluid Dyn. (1989–1993) 3 (7) (1991) 1760–1765.
[33] B. Semlitsch, M. Mihaescu, L. Fuchs, E.J. Gutmark, Influence of sub-grid scale models for large eddy simulations on the acoustic noise production in jets, in: 14th European Turbulence Conference, 1–4 September 2013, Lyon, France, 2013.
[34] P. Moin, J. Kim, Numerical investigation of turbulent channel flow, J. Fluid Mech. 118 (1982) 341–377.
[35] D.P. Rizzetta, M.R. Visbal, Large-eddy simulation of supersonic cavity flow fields including flow control, AIAA J. 41 (8) (2003) 1452–1462.
[36] J.E. Ffowcs Williams, D.L. Hawkings, Sound generated by turbulence and surfaces in arbitrary motion, Philos. Trans. R. Soc. Lond. Ser. A, Math. Phys. Sci. 264 (1969) 321–342.
[37] C. Xu, Y. Mao, Passive control of centrifugal fan noise by employing open-cell metal foam, Appl. Acoust. 103 (2016) 10–19.
[38] P.D. Lax, B. Wendroff, Difference schemes for hyperbolic equations with high order of accuracy, Commun. Pure Appl. Math. 17 (3) (1964) 381–398.
[39] A.J. Torregrosa, P. Fajardo, A. Gil, R. Navarro, Development of non-reflecting boundary condition for application in 3D computational fluid dynamics codes, Eng. Appl. Comput. Fluid Mech. 6 (3) (2012) 447–460.
[40] C. Wang, L. Huang, Passive noise reduction for a contra rotating fan, J. Turbomach. 137 (3) (2015) 031007.
[41] J. Xiang, J.U. Schlüter, F. Duan, Towards simulation of NASA35 axial compressor, Aircr. Eng. 7 (6) (2015) 571–583.
[42] A. Suman, R. Kurz, N. Aldi, M. Morini, K. Brun, M. Pinelli, P.R. Spina, Quantitative computational fluid dynamics analyses of particle deposition on a transonic axial compressor blade—part I: particle zones impact, J. Turbomach. 137 (2) (2015) 021009.
[43] B.B. Hu, H. OuYang, Y.D. Wu, G.Y. Jin, X.Q. Qiang, Z.H. Du, Numerical prediction of the interaction noise radiated from an axial fan, Appl. Acoust. 74 (4) (2013) 544–552.
[44] C. Abdelmadjid, S.A. Mohamed, B. Boussad, CFD analysis of the volute geometry effect on the turbulent air flow through the turbocharger compressor, Energy Proc. 36 (2013) 746–755.
[45] I. Shahin, M. Gadala, M. Alqaradawi, O. Badr, Large eddy simulation for a deep surge cycle in a high-speed centrifugal compressor with vaned diffuser, J. Turbomach. 137 (10) (2015) 101007.
[46] T. Halawa, M. Alqaradawi, M.S. Gadala, I. Shahin, O. Badr, Numerical investigation of rotating stall in centrifugal compressor with vaned and vaneless diffuser, Int. J. Therm. Sci. 24 (4) (2015) 323–333.
[47] M.P. Wernet, Development of digital particle imaging velocimetry for use in turbomachinery, Exp. Fluids 28 (2) (2000) 97–115.
[48] L.M. Larosiliere, G.J. Skoch, P.S. Prahst, Aerodynamic Synthesis of a Centrifugal Impeller Using CFD and Measurements, National Aeronautics and Space Administration, 1997.
[49] P. Lafon, S. Caillaud, J.P. Devos, C. Lambert, Aero acoustical coupling in a ducted shallow cavity and fluid/structure effects on a steam line, J. Fluids Struct. 18 (6) (2003) 695–713.
[50] A. Broatch, J. Galindo, R. Navarro, J. García-Tíscar, Methodology for experimental validation of a CFD model for predicting noise generation in centrifugal compressors, Int. J. Heat Fluid Flow 50 (2014) 134–144.
[51] J. Galindo, A. Tiseira, R. Navarro, M.A. López, Influence of tip clearance on flow behavior and noise generation of centrifugal compressors in near-surge conditions, Int. J. Heat Fluid Flow 52 (2015) 129–139.
[52] S.G. Mallat, A theory for multi-resolution signal decomposition: the wavelet representation, IEEE Trans. Pattern Anal. Mach. Intell. 11 (7) (1989) 674–693.
[53] D.L. Donoho, I.M. Johnstone, Adapting to unknown smoothness via wavelet shrinkage, J. Am. Stat. Assoc. 90 (432) (1995) 1200–1224.
[54] M. Darvish, B. Tietjen, D. Beck, S. Frank, Tonal noise reduction in a radial fan with forward-curved blades, in: ASME Turbo Expo 2014: Turbine Technical Conference and Exposition, American Society of Mechanical Engineers, June 2014, V01AT10A020.
[55] C. Wagner, T. Huttl, P. Sagaut, Large-Eddy Simulation for Acoustics, Cambridge University Press, 2007.
[56] I.W. Selesnick, R.G. Baraniuk, N.C. Kingsbury, The dual-tree complex wavelet transform, IEEE Signal Process. Mag. 22 (6) (2005) 123–151.
[57] D.L. Donoho, I.M. Johnstone, Adapting to unknown smoothness via wavelet shrinkage, J. Am. Stat. Assoc. 90 (432) (1995) 1200–1224.